The Astrophysical Journal Letters, 990:L46 (15pp), 2025 September 10 https://doi.org/10.3847/2041-8213/adfd49

Kilonova Constraints for the LIGO/Virgo/KAGRA Neutron Star Merger Candidate S250206dm: GW-MMADS Observations

Lei Hu[1], Tomás Cabrera[1], Antonella Palmese[1], James Freeburn[2,3], Mattia Bulla[4,5,6], Igor Andreoni[7], Xander J. Hall[1], Brendan O'Connor[1], Ariel Amsellem[1], Clécio R. Bom[8], Malte Busmann[9], Jennifer Fabà[9], Julius Gassert[9], Sena Kalabalik[9], Keerthi Kunnumkai[1], Daniel Gruen[9,10], Luidhy Santana-Silva[8], André Santos[8], Tomás Ahumada[11], Jonathan Carney[7], Michael W. Coughlin[12], Xingzhuo Chen[13,14], K. E. Saavik Ford[15,16,17], Daniel E. Holz[18,19,20,21], Mansi M. Kasliwal[11], Ignacio Magaña Hernandez[1], Cassidy Mihalenko[3,22], Rosalba Perna[23], Arno Riffeser[9,24], Christoph Ries[9], Lena Schnappinger[9], Michael Schmidt[9], Julian Sommer[9], Sarah Teague[7], Pablo Vega[9], Olga Volchansky[25], Lifan Wang[13], and Yajie Zhang[9]

[1] McWilliams Center for Cosmology and Astrophysics, Department of Physics, Carnegie Mellon University, 5000 Forbes Avenue, Pittsburgh, PA 15213, USA; leihu@andrew.cmu.edu
[2] Centre for Astrophysics and Supercomputing, Swinburne University of Technology, John Street, Hawthorn, VIC 3122, Australia
[3] ARC Centre of Excellence for Gravitational Wave Discovery (OzGrav), John Street, Hawthorn, VIC 3122, Australia
[4] Department of Physics and Earth Science, University of Ferrara, via Saragat 1, I-44122 Ferrara, Italy
[5] INFN, Sezione di Ferrara, via Saragat 1, I-44122 Ferrara, Italy
[6] INAF, Osservatorio Astronomico d'Abruzzo, via Mentore Maggini snc, 64100 Teramo, Italy
[7] Department of Physics and Astronomy, University of North Carolina at Chapel Hill, Chapel Hill, NC 27599-3255, USA
[8] Centro Brasileiro de Pesquisas Físicas, Rua Dr. Xavier Sigaud 150, 22290-180 Rio de Janeiro, RJ, Brazil
[9] University Observatory, Faculty of Physics, Ludwig-Maximilians-Universität München, Scheinerstr. 1, 81679 Munich, Germany
[10] Excellence Cluster ORIGINS, Boltzmannstr. 2, 85748 Garching, Germany
[11] Division of Physics, Mathematics and Astronomy, California Institute of Technology, Pasadena, CA 91125, USA
[12] School of Physics and Astronomy, University of Minnesota, Minneapolis, MN 55414, USA
[13] George P. and Cynthia Woods Mitchell Institute for Fundamental Physics & Astronomy, Texas A. & M. University, Department of Physics and Astronomy, 4242 TAMU, College Station, TX 77843, USA
[14] Texas A&M Institute of Data Science John R. Blocker Building, Suite 227155 Ireland Street, TAMU 3156, College Station, TX 77843-3156, USA
[15] Center for Computational Astrophysics, Flatiron Institute, 162 5th Avenue, New York, NY 10010, USA
[16] Department of Astrophysics, American Museum of Natural History, New York, NY 10024, USA
[17] Department of Science, BMCC, City University of New York, New York, NY 10007, USA
[18] Kavli Institute for Cosmological Physics, University of Chicago, Chicago, IL 60637, USA
[19] Enrico Fermi Institute, University of Chicago, Chicago, IL 60637, USA
[20] Department of Physics, University of Chicago, Chicago, IL 60637, USA
[21] Department of Astronomy and Astrophysics, University of Chicago, Chicago, IL 60637, USA
[22] School of Natural Sciences, University of Tasmania, Private Bag 37, Hobart, Tasmania, 7001, Australia
[23] Department of Physics and Astronomy, Stony Brook University, Stony Brook, NY 11794-3800, USA
[24] Max-Planck-Institut für Extraterrestrische Physik, Giessenbachstraße 1, 85748 Garching, Germany
[25] Department of Orthopaedics, University of North Carolina at Chapel Hill, Chapel Hill, NC 27599-3255, USA
Received 2025 June 25; revised 2025 August 14; accepted 2025 August 19; published 2025 September 3

Abstract

Gravitational-wave (GW) neutron star mergers with an associated electromagnetic counterpart constitute powerful probes of binary evolution, the production sites of heavy elements, general relativity, and the expansion of the Universe. Only a handful of candidate GW binary mergers during the fourth LIGO/Virgo/KAGRA observing run (O4) so far are believed to include a neutron star. We present optical–near-infrared follow-up observations of the candidate neutron star–black hole GW merger S250206dm. This is the first high-significance mass-gap neutron star–black hole candidate observed by multiple GW detectors (thus having a significantly smaller sky localization than one-detector events), offering the first opportunity to effectively follow up a GW event of this kind. Our GW MultiMessenger Astronomy DECam Survey (GW-MMADS) campaign consisted of a wide-field search using the Dark Energy Camera (DECam) and T80-South (T80S), as well as galaxy-targeted observations using the Southern Astrophysical Research (SOAR) imager and the Fraunhofer Telescope at Wendelstein Observatory. No viable kilonova counterpart was found in our observations. We use our observation depths to place competitive constraints on kilonova models similar to or brighter than the GW170817 kilonova AT 2017gfo within our observed fields, ruling out 100% of such models with SOAR galaxy-targeted observations and ∼43% (48%) with DECam (DECam and T80S).

Unified Astronomy Thesaurus concepts: Gravitational wave astronomy (675); Transient detection (1957)

1. Introduction

Multimessenger observations of gravitational-wave (GW) events can enable a wide range of scientific analyses, from stellar evolution studies to measurements of fundamental physical and cosmological parameters. This has been exemplarily demonstrated with the first multimessenger GW detection,

GW170817 (B. P. Abbott et al. 2017), observed by the Laser Interferometer Gravitational-wave Observatory (LIGO; LIGO Scientific Collaboration 2015), Virgo (F. Acernese et al. 2014), and a large number of multiwavelength EM facilities (LIGO Scientific Collaboration et al. 2017). GW events arising from binary neutron star (BNS) or black hole–neutron star (BHNS) mergers can give rise to a variety of electromagnetic (EM) counterparts at different wavelengths. Notably, in the optical to infrared range, these objects can emit EM radiation from a kilonova (e.g., B. D. Metzger 2019), a transient powered by the radioactive decay of heavy *r*-process elements produced in the merger ejecta (J. M. Lattimer & D. N. Schramm 1974). At the time of writing, only one high-confidence BNS GW merger has been detected since GW170817–GW190425 (B. P. Abbott et al. 2020)—for which no EM counterpart was identified, likely due to its larger distance and sky localization (M. W. Coughlin et al. 2019).

Depending on the compact objects' masses, the neutron star equation of state (EOS), and the black hole spin, BHNS mergers can also give rise to a kilonova (F. Foucart 2012; K. Kyutoku et al. 2013; D. Kasen et al. 2015; K. Kawaguchi et al. 2016; R. Fernández et al. 2017). BHNS binaries in which the black hole has a relatively low mass are more likely to produce a kilonova, as the neutron star can be tidally disrupted, ejecting neutron-rich material whose radioactive decay powers the observable transient. In contrast, higher-mass black holes typically cause the neutron star to plunge directly into the black hole, resulting in negligible EM emission. Prior to LIGO and Gaia observations, EM-based studies suggested that stellar-mass black holes typically have masses above $5\,M_{\odot}$, leading to the conjecture of a so-called "mass gap" between the neutron star and the black hole population in the range of 3–5 $M_{\odot}$. The potential involvement of black holes within this mass gap revives the prospects for multimessenger observations of BHNS mergers, as tidal disruption—and thus EM emission—is more favorable in this regime. In contrast, previous follow-up campaigns for BHNS mergers with black hole masses above $5\,M_{\odot}$ have not yielded any confirmed EM counterparts (S. Anand et al. 2021). During the ongoing fourth observing run (O4; 2023–2025) of LIGO/Virgo/KAGRA, the first BHNS candidate likely hosting a mass-gap black hole was identified—GW230529 (The LIGO Scientific Collaboration et al. 2024). The existence of such systems renders BHNS mergers invaluable sources for multimessenger kilonova detections (K. Kunnumkai et al. 2024a, 2024b). However, only one GW detector was online at the time of GW230529, resulting in poor sky localization and challenging most EM follow-up efforts. While the nondetection of a gamma-ray burst enabled constraints on the jet properties (S. Ronchini et al. 2024), kilonova modeling was only possible over a small fraction of the sky, yielding limited constraints (M. Pillas et al. 2025).

On 2025 February 6 at 21:25:30 UT, the LIGO and Virgo detectors observed S250206dm (LIGO Scientific Collaboration et al. 2025a, 2025c, 2025b, 2025d), a candidate GW event with a marginalized luminosity distance of 373 ± 104 Mpc and a sky localization of 38 and 547 deg^2 at a 50% and 90% credible interval, respectively. Based on the latest `pycbc` alert estimates, S250206dm has a 55% probability of being a BHNS merger and a 37% chance of being a BNS merger. Notably, there is a 62% probability of containing a black hole in the mass gap and a 30% chance of having disrupted material outside of the black hole's innermost stable circular orbit (ISCO). Collectively, these estimates make S250206dm the most promising multimessenger candidate of the O4 run to date. Fermi-GBM partially covered the localization region of S250206dm around the GW event time, while no associated gamma-ray emission was detected within the observed area (O. Mukherjee et al. 2025). Prior to S250206dm, no previous GW alerts during O4 have been confidently associated with any EM counterpart (T. Ahumada et al. 2024; T. Cabrera et al. 2024; P. Darc et al. 2025; M. Pillas et al. 2025).

In this work, we present the follow-up campaign carried out as part of the Gravitational Wave MultiMessenger DECam Survey (GW-MMADS; Proposal ID 2023B-851374; PI. Andreoni & Palmese), in coordination with other facilities, namely the Southern Astrophysical Research (SOAR) 4 m telescope, the T80S 0.8 m telescope, the Wendelstein 2.1 m telescope, and the South African Large Telescope (SALT). A companion work by T. Ahumada et al. (2025a) presents the follow-up campaign and results from the Zwicky Transient Facility (ZTF), which—combined with ours observations—covers the majority of the high-probability localization region S250206dm. Additionally, near-infrared constraints on this event are reported by D. Frostig et al. (2025). In Section 2 we describe our follow-up strategy and observations. In Section 3 we present the candidates identified from the campaign. In Section 4 we constrain kilonova models based on our findings, along with some discussion of the results in Section 5. In Section 6 we report our conclusions.

2. Observations

2.1. Galaxy-targeted Search with SOAR/Goodman

Approximately 9 hr after the GW trigger, we conducted a galaxy-targeted search using the Goodman High Throughput Spectrograph (J. C. Clemens et al. 2004) mounted on the SOAR 4.1 m telescope,[26] operated in imaging mode for target-of-opportunity (ToO) observations (PI. Andreoni). We observed 33 galaxies located in the highest-probability region of S250206dm in both *g* and *i* bands (J. Freeburn et al. 2025a), with corresponding pointings shown in Figure 1. These galaxies were selected by cross-matching the sky localization with the NASA/IPAC Extragalactic Database (NED) Local Volume Sample (NED-LVS; D. O. Cook et al. 2023), taking into account the NED galaxy list of S250206dm from D. O. Cook et al. (2025a). Data acquisition started on 2025 February 7 at 06:36:12.51 UT and lasted for about 2 hr, reaching typical depths of 22.2 and 21.7 mag for *g* and *i* bands, respectively. On 2025 February 9, SOAR revisited 30 galaxies in the highest-probability region, conducting *i*-band observations from 06:48 UT to 09:18 UT with comparable depths to the previous night (J. Freeburn et al. 2025b). The details of SOAR pointings are available in TreasureMap.[27]

2.2. Galaxy-targeted Search with FTW/3KK

In the Northern Hemisphere, a galaxy-targeted search for the optical and near-infrared counterpart of S250206dm was initialized with the Three Channel Imager (3KK; F. Lang-Bardl et al. 2016) on the 2.1 m Fraunhofer Telescope at Wendelstein Observatory (FTW; U. Hopp et al. 2014). The 3KK imager

[26] https://noirlab.edu/science/programs/ctio/telescopes/soar-telescope
[27] https://treasuremap.space/alerts?graceids=S250206dm

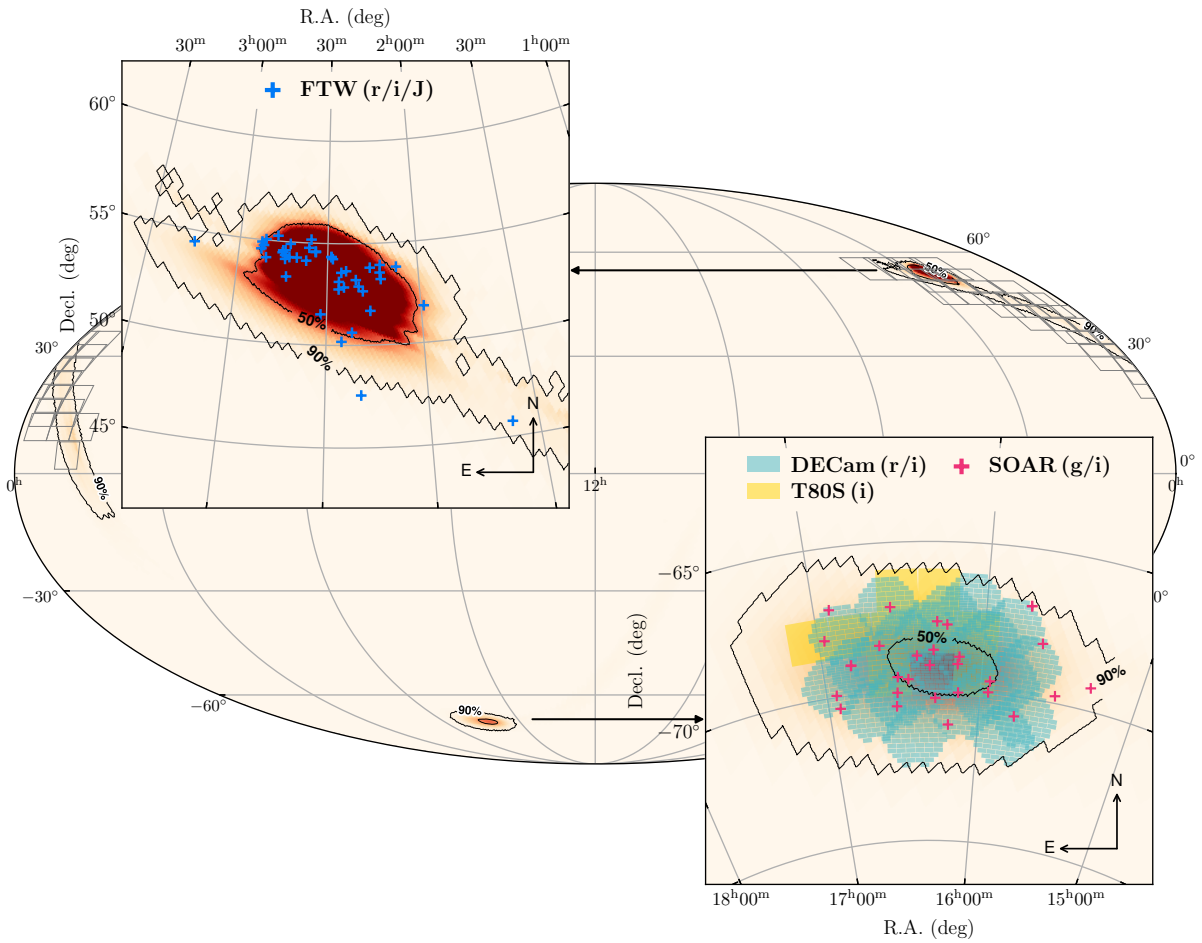

Figure 1. Localization region of S250206dm overlapped with the footprints of GW-MMADS follow-up observations. The upper and lower inset panels show zoomed-in views of two lobes of the LVK sky map with high probability, located in the Northern and Southern Hemispheres, respectively. For reference, we also overlay in gray the sky tiles in the northern lobe used for ZTF observations of S250206dm (T. Ahumada et al. 2025a).

enables simultaneous observations in three channels with a $7' \times 7'$ field of view. For S250206dm, we configured the *r*, *i*, and *J* bands for blue, red, and near-infrared channels, respectively. Beginning 19 hr after the event, on 2025 February 7 at 19:00:21 UT, FTW/3KK commenced observations on 50 targets selected from the NED Galaxies in the Localization Volume in D. O. Cook et al. (2025a). The selection was based on ranking galaxies by the product of the 3D localization probability and Wide-field Infrared Survey Explorer W1 luminosity, retaining only targets located in the Northern Hemisphere (with decl. > 0). On the same night, FTW/3KK also observed the 90% localization region of EP-WXT trigger 01709131361, which lies within the 70% localization of S250206dm, beginning at 2025 February 7 at 17:52:05 UT (20.4 hr after the merger; M. Busmann et al. 2025a). On 2025 February 8, FTW observations proceeded with 12 targets from the updated NED Galaxies in the Localization Volume (D. O. Cook et al. 2025b), including 11 from the original sample and one new addition. We also followed up the candidate AT 2025baz reported by ZTF (T. Ahumada et al. 2025b). In the subsequent weeks, intermittent follow-ups were conducted on a subset of transient candidates. Figure 1 shows the footprints of the galaxy-targeted search with the FTW/3KK observations overlaid on the the LIGO/Virgo/KAGRA (LVK) sky map of S250206dm. The details of FTW pointings are available in TreasureMap (see footnote 27); those affected by poor weather and resulting in unsuccessful data reduction are not included.

2.3. DECam Search

Since S250206dm occurred on the day the DECam camera was taken off the Blanco 4 m telescope at Cerro Tololo Inter-American Observatory (CTIO) for engineering, DECam was unavailable during the early follow-up phase of the event. GW-MMADS commenced ToO observations with DECam immediately following the camera's reinstallation. The DECam observations began on 2025 February 13 at 06:15:00.30 UT—approximately 6 days after the binary merger—and lasted for 3 hr.

On the first night, we adopted an exposure sequence of *i*–*r*–*i* band for each pointing, with exposure times of 60 s in the *r* band and 140 s in the *i* band, reaching typical depths of 22.6 and 23.0 mag, respectively. The relatively deep *i*-band observations were designed to enhance the detection sensitivity to a potential red counterpart associated with the GW event at this phase. To minimize contamination from moving objects, we maintained a typical gap of 90 minutes between two *i*-band observations of each pointing. As shown in Figure 1, we used 23 pointings to fully cover the 50% probability region and the majority of the 90% probability region in the Southern Hemisphere. We note that our DECam coverage is slightly redundant, particularly within the 50%

probability region, as the pointings were intentionally selected with significant overlap to mitigate the risk of candidate loss due to CCD chip gaps. The details of DECam pointings are available in TreasureMap (see footnote 27).

We repeated the observations on the following night using the same strategy, with a slightly longer *r*-band exposure of 70 s, beginning on 2025 February 14 at 06:22:17.23 UT. DECam follow-up observations resumed 3 days later, starting on 2025 February 17 at 07:48:50.60 UT, consisting of a single round of *i*-band imaging with the same 140 s exposure time. The final DECam observations were conducted on 2025 February 27, beginning at 07:04:25.54 UT, using the same *i*–*r*–*i* exposure sequence as the first night, but with increased exposure times of 280 s in the *i* band and 70 s in the *r* band.

2.4. T80-South Search

We conducted observations using the T80Cam on board the T80-South Telescope located at CTIO, triggered via a ToO approximately 9 hr after the GW alert. We observed nine tiles inside the lobe located in the Southern Hemisphere, using 300 s exposures in the *i* band. This observation strategy provided a total coverage of 18 deg^2 during the night. The choice of exposure time and filter was optimized to enhance sensitivity to a potential kilonova emission expected in the early times post-merger. The tiling of the GW sky map was performed using `Teglon` (D. A. Coulter 2021), an open-source tool developed for optimized planning of EM follow-up observations of GW events. `Teglon` improves on the original LVK localization by incorporating a completeness metric derived using a galaxy catalog—in our case, the GLADE catalog (G. Dálya et al. 2018)—to estimate the spatial distribution of potential host galaxies in three dimensions. This results in a reweighted localization map that accounts for galaxy density and distance priors. `Teglon` then subdivides the updated probability map into fields corresponding to the field of view of the T80-South telescope, generating a ranked list of pointings for observations. However, after our observing sequence was submitted to the T80-South queue, an updated version of the GW sky map was released. This revised localization slightly shifted the position of the highest-probability region within the southern lobe. As a result, a fraction of the most probable sky area was not included in our executed pointings.

3. Candidates

3.1. Candidates from SOAR/Goodman

We performed image differencing analysis for the SOAR/Goodman observations using Saccadic Fast Fourier Transform (SFFT[28]; L. Hu et al. 2022). Two approaches were implemented to search for a potential counterpart on the difference images: (i) using the SOAR/Goodman observations from the first epoch (2025 February 7) as science images and the observations from the second epoch (2025 February 9) as templates (J. Freeburn et al. 2025b), and (ii) subtracting SOAR images of both epochs using the best available archival DECam images as templates. All SOAR/Goodman images were photometrically calibrated to SkyMapper DR4 (C. A. Onken et al. 2024). Following visual inspection, AT 2025ber was the only candidate that remained (J. Freeburn et al. 2025b). However, near-infrared follow-up by NEWFIRM on 2025 February 12 yielded a deep nondetection (D. A. Coulter et al. 2025), suggesting that it is likely a spurious source or unrelated moving object.

3.2. Candidates from FTW/3KK

FTW/3KK data were reduced using a custom analysis pipeline based on C. A. Gössl & A. Riffeser (2002) and M. Busmann et al. (2025b), which applies standard image processing, including common detector-level corrections. The calibrated images were subsequently stacked using the AstrOmatic software suite (E. Bertin & S. Arnouts 1996; E. Bertin et al. 2002; E. Bertin 2006). To search for variable sources, image differencing analysis was conducted on the stacked images using SFFT (L. Hu et al. 2022), employing FTW/3KK images taken from the same field as reference, mostly at a late phase in March. No variability was detected upon careful inspections, except for a nuclear transient candidate[29] at R.A. = 02:22:00.28, decl. = +50:37:37.10. However, a brightening of the transient candidate was detected on March 8, which does not match the expected photometric behavior of a kilonova, suggesting that it may be related to AGN variability. For the EP-WXT trigger 01709131361, we did not identify any objects that brightened with respect to archival Legacy Survey *r*-band data or Two Micron All Sky Survey *J*-band data, except for the flaring star reported by A. J. Levan et al. (2025), which is likely the progenitor of the EP-WXT trigger.

3.3. Candidates from DECam

We analyzed the DECam observations using our GPU-enabled image differencing pipeline for rapid transient detection and photometry (L. Hu et al. 2025, in preparation), built on the high-efficiency SFFT algorithm (L. Hu et al. 2022). Each science image was subtracted against archival DECam reference images using SFFT. A total of 37 candidates passed the automated filtering and subsequent visual inspection, several of which were circulated via General Coordinates Network (GCN; T. Cabrera et al. 2025). However, no compelling candidates meeting all vetting criteria were identified in the DECam observations for S250206dm. We provide a detailed description of the DECam candidate filtering process and results in Appendix A; a full account of the DECam transient pipeline is deferred to L. Hu et al. (2025, in preparation). SALT spectroscopic follow-up observations were conducted for four of these DECam candidates, with further observational details presented in Appendix B.

3.4. Candidates from T80-South

All exposures acquired with T80-South were processed using the S-PLUS Transient Extension Program pipeline (A. Santos et al. 2024). The raw images from the T80-South telescope went through a prereduction process that includes bias subtraction, flat-field correction, overscan removal, and image trimming. Once preprocessed, all images go through the reduction pipeline, which applies a nonlinear astrometric correction over the images and performs zero-point calibrations. In order to find variable sources, we perform difference imaging using `hotpants` (A. Becker 2015) and DECam

[28] https://github.com/thomasvrussell/sfft

[29] Internal name S250206dm_022200_p503737.

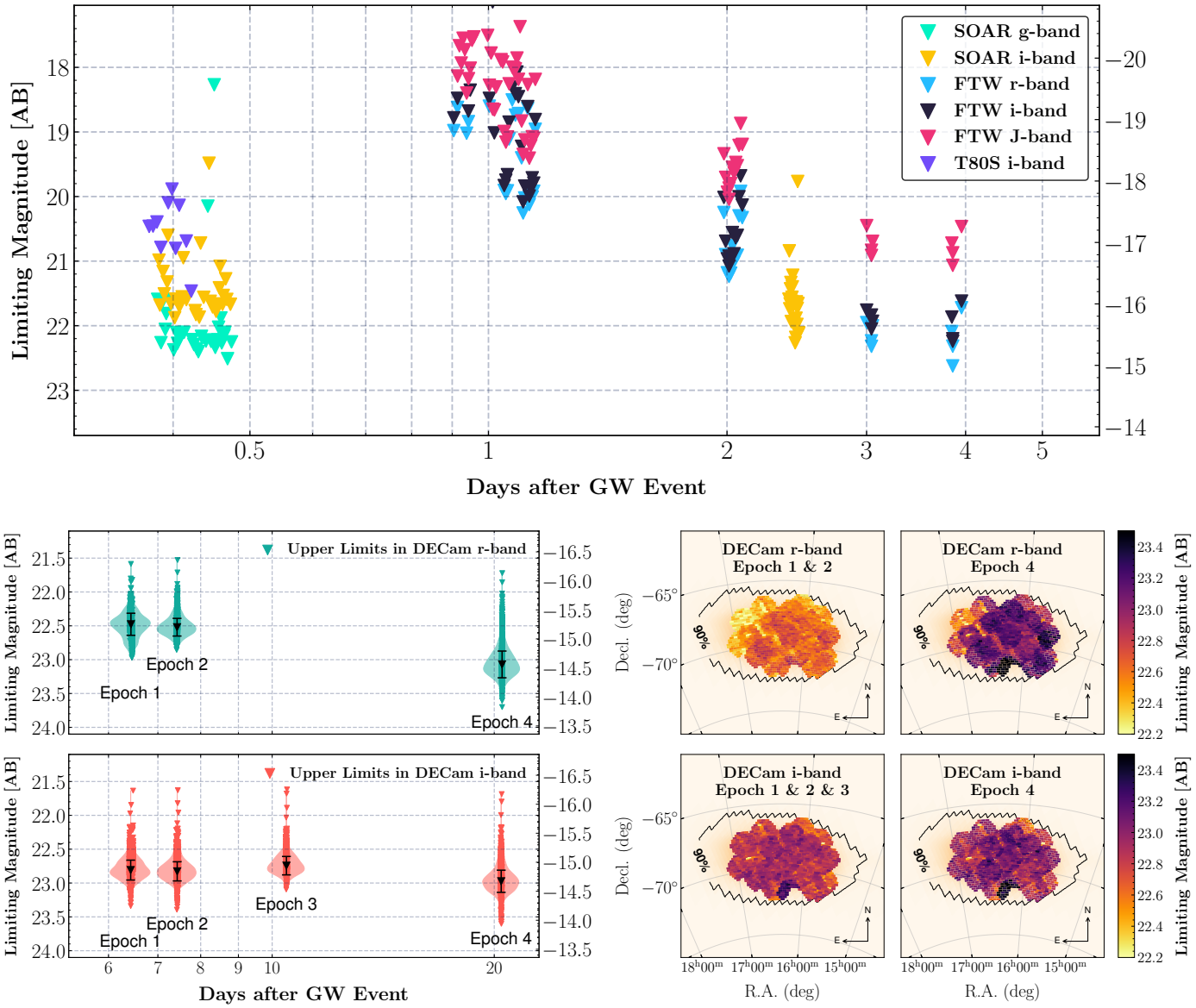

Figure 2. Limiting magnitudes of GW-MMADS observations for S250206dm. Upper panel: limiting magnitudes of early (<5 days from trigger) observations as a function of time for S250206dm. Colored triangles represent upper limits obtained with different instruments and filters, including SOAR in g/i bands, T80S in i band, and Wendelstein 3KK in $r/i/J$ bands. For reference, the right y-axis converts apparent magnitudes to absolute magnitudes assuming that S250206dm is at 373 Mpc. Lower left panels: DECam limiting magnitudes as a function of time after the GW event for DECam r band (top) and i band (bottom). For each epoch, a violin plot is overlaid to represent the distribution of limiting magnitudes across the observations, while a black triangle marks the median upper limit, with error bars indicating the standard deviation. Again, the right-hand y-axis presents absolute magnitudes for a distance of 373 Mpc. Lower right panels: spatial variation of limiting magnitudes across the DECam coverage for r band (top) and i band (bottom). For visualization purposes, we grouped epochs with similar depth distributions (e.g., epochs 1 and 2 in the r band) and presented them in a single panel.

archival images as templates. After image subtraction and inspection of detailed candidate vetting, no transient sources consistent with an EM counterpart were identified within our search region. Given our criteria for finding viable candidates for the following epoch, observations on the following night were not acquired.

4. Upper Limits and Kilonova Constraints

4.1. Upper Limits and Completeness

Figure 2 shows the 5σ limiting magnitudes we measured on the difference images for SOAR, FTW, DECam, and T80S observations. We employ these measurements to derive constraints on kilonova parameters using both BNS and BHNS kilonova models. Based on the three-dimensional localization probability using W1-band luminosity from D. O. Cook et al. (2025a), we performed an approximate estimate to assess the likelihood that our galaxy-targeted observations covered the true host of S250206dm. The SOAR observations cover approximately 1.3% of the probability, and the FTW/3KK observations cover about 1.5%. The estimation is performed against a luminosity function, capturing a true completeness including the 3D localization of the individual galaxies (J. Gassert et al. 2025, in preparation). It is based on the idea of using luminosities (here in r band/W1 band) as a proxy for stellar mass. By using a luminosity function as expectation and comparing the true luminosities of the individual galaxies in the target catalog, we estimate the

completeness in the specific 3D volume of the GW event. Therefore, this estimate inherently accounts for galaxy catalog incompleteness, by comparing the expected luminosity distribution to the actual contents of the catalog. This approach not only incorporates the luminosity function as is but also weighs the contributions based on their 3D localization such that galaxies with high luminosity in the outskirts of the localization volumes count less toward the completeness compared to similar galaxies (in terms of luminosity) in a high-probability region. For consistency, we use the 90% credible region of the GW localization in these calculations, a common threshold in GW follow-up. The described procedure is designed to be robust against uncertainties in the GW localization, as long as the true host lies within the 90% credible region. If the true host falls outside, the estimate will incorrectly suggest a nonzero chance of detection. Complementing these targeted observations, the DECam observations covered a broader region, comprising 9.3% of the cumulative localization probability in the LVK sky map. T80S observations cover 4.9% of the cumulative localization probability from the LVK sky map, with 4.5% overlapping the DECam footprint.

4.2. Kilonova Models

We use state-of-the-art kilonova models computed with the 3D Monte Carlo radiative transfer code POSSIS (M. Bulla 2019, 2023), as also done in T. Ahumada et al. (2025a). In summary, ejecta are modeled under the assumption of axial symmetry and are composed of two components (E. Nakar 2020): the first is ejected on dynamical timescales during the merger ("dynamical ejecta"), while the second is launched afterward from an accretion disk formed around the merger remnant ("disk wind ejecta"). Angular profiles for the ejecta density and composition are implemented following suggestions from numerical relativity simulations, which lead to a viewing angle dependence of the signal. The BNS kilonova dynamical ejecta follow a density $\rho \propto \sin^2\theta$ and an electron fraction $Y_e(\theta) \propto \cos^2\theta$ profile, where θ is the polar angle with respect to the binary angular momentum, while the wind ejecta have uniform Y_e and spherically symmetric density (A. Perego et al. 2017; D. Radice et al. 2018; C. N. Setzer et al. 2023). For what concerns the BHNS models, the dynamical ejecta are more strongly focused around the merger plane —$\rho \propto 1/\{1 + \exp[-20\,(\theta - 1.2)]\}$—and their electron fraction is fixed to $Y_e = 0.1$, whereas the wind ejecta are spherical and have a flat distribution of Y_e values between 0.2 and 0.3 (K. Kawaguchi et al. 2020, and references therein). The viewing angle dependence is explored by computing kilonova observables for 11 different viewing angles equally spaced in cosine from the merger plane ($\cos\theta_{\rm obs} = 0$, edge-on case) to the pole ($\cos\theta_{\rm obs} = 1$, face-on). The heating rates are updated compared to previous work and consistent with those from S. Rosswog & O. Korobkin (2024).

Inspired by S. Anand et al. (2023), a grid of 3072 BNS kilonova models is generated by varying the mass, velocity, and electron fraction of both ejecta components within ranges suggested by numerical relativity simulations: dynamical ejecta mass $M_{\rm dyn} = (0.001, 0.005, 0.01, 0.02)\,M_\odot$, mass-weighted dynamical ejecta velocity $\bar{v}_{\rm dyn} = (0.12, 0.15, 0.2, 0.25)c$, mass-weighted dynamical ejecta electron fraction $\bar{Y}_{e,\rm dyn} = (0.15, 0.20, 0.25, 0.30)$, wind ejecta mass $M_{\rm wind} = (0.01, 0.05, 0.09, 0.13)\,M_\odot$, mass-weighted wind ejecta velocity $\bar{v}_{\rm wind} = (0.03, 0.05, 0.10, 0.15)c$, and fixed wind ejecta electron fraction $Y_{e,\rm wind} = (0.20, 0.30, 0.40)$.

Following L. W. P. Mathias et al. (2024), a separate grid of 108 BHNS kilonova models is constructed by varying the masses of the two compact objects, the black hole spin, and the EOS, with the following choices: $M_{\rm NS} = (1.2, 1.4, 1.6, 1.8)\,M_\odot$, $M_{\rm BH} = (4.0, 6.0, 8.0)\,M_\odot$, $\chi_{\rm BH} = (0.0, 0.3, 0.6)$, and EOS (from stiff to soft) = (DD2, AP3, SFHo+HΔ) (A. Akmal et al. 1998; M. Hempel & J. Schaffner-Bielich 2010; A. Drago et al. 2014). Numerical relativity fitting formulae are used to determine the properties of the ejecta, with only 37 out of 108 BHNS models leading to material being ejected and therefore resulting in a kilonova signal. When taking into account the viewing angle as an additional free parameter, the total number of simulated kilonovae in the two grids is 33,792 and 407, respectively.

A uniform grid of $\cos\theta_{\rm obs}$ is adopted to account for different viewing angles for both BHNS and BNS models. However, this setup does not reflect the expected probability distribution of viewing angles for such binary systems. Given the absence of specific constraints on the inclination with respect to the line of sight for this event, here we incorporate a prior distribution of viewing angles of compact binary coalescences introduced by B. F. Schutz (2011), which peaks at $\sim 30^\circ$. We assign to each model a weight corresponding to the probability of its viewing angle under the Schutz distribution. Throughout this paper, all reported fractions of model constraints are weighted accordingly to account for this effect.

4.3. Kilonova Constraints

This subsection presents our kilonova model constraints based on our upper limits from follow-up observations. We first briefly summarize the results shown in Figures 3 and 4, followed by separate descriptions on the BHNS and BNS scenarios to illustrate their distinct constraints.

In Figure 3 we show light curves from our model grids (across different viewing angles) at a distance of 323 Mpc, the mean of the luminosity distance posterior distribution over the southern sky lobe of high probability covered by DECam and SOAR. The 1σ luminosity distance constraint around this median is 82 Mpc in this region. We compare these light curves with our upper limits and show in color the light curves that are excluded by our nondetections. Milky Way extinction at the location ($E(B - V) = 0.1 \pm 0.02$ mag using J. A. Cardelli et al. 1989) is accounted for in the observed upper limits before evaluating model viability.

In Figure 4 we show how the excluded models translate into constraints on physical parameters. As our fiducial scenario, we consider the case where the viewing angle is off-axis with $\cos(\theta) = 0.9$ (the grid point nearest to the peak of the Schutz distribution of viewing angles) and present the percentage of models ruled out in each parameter combination. The value of $\cos(\theta) = 0.9$ corresponds to a viewing angle of $\sim 26^\circ$, which is close to both the GW170817 viewing angle (e.g., K. P. Mooley et al. 2018; R. Margutti & R. Chornock 2021; A. Palmese et al. 2024) and the expected peak of the distribution of angles from an observed population of GW events (B. F. Schutz 2011). To account for the uncertainty in the event's distance, we sample 256 values from the posterior distribution of the luminosity distance over the southern sky lobe of high probability (with a mean distance of 323 Mpc). The exclusion fraction is computed at each sampled distance and then averaged to yield the overall constraint illustrated in Figure 4.

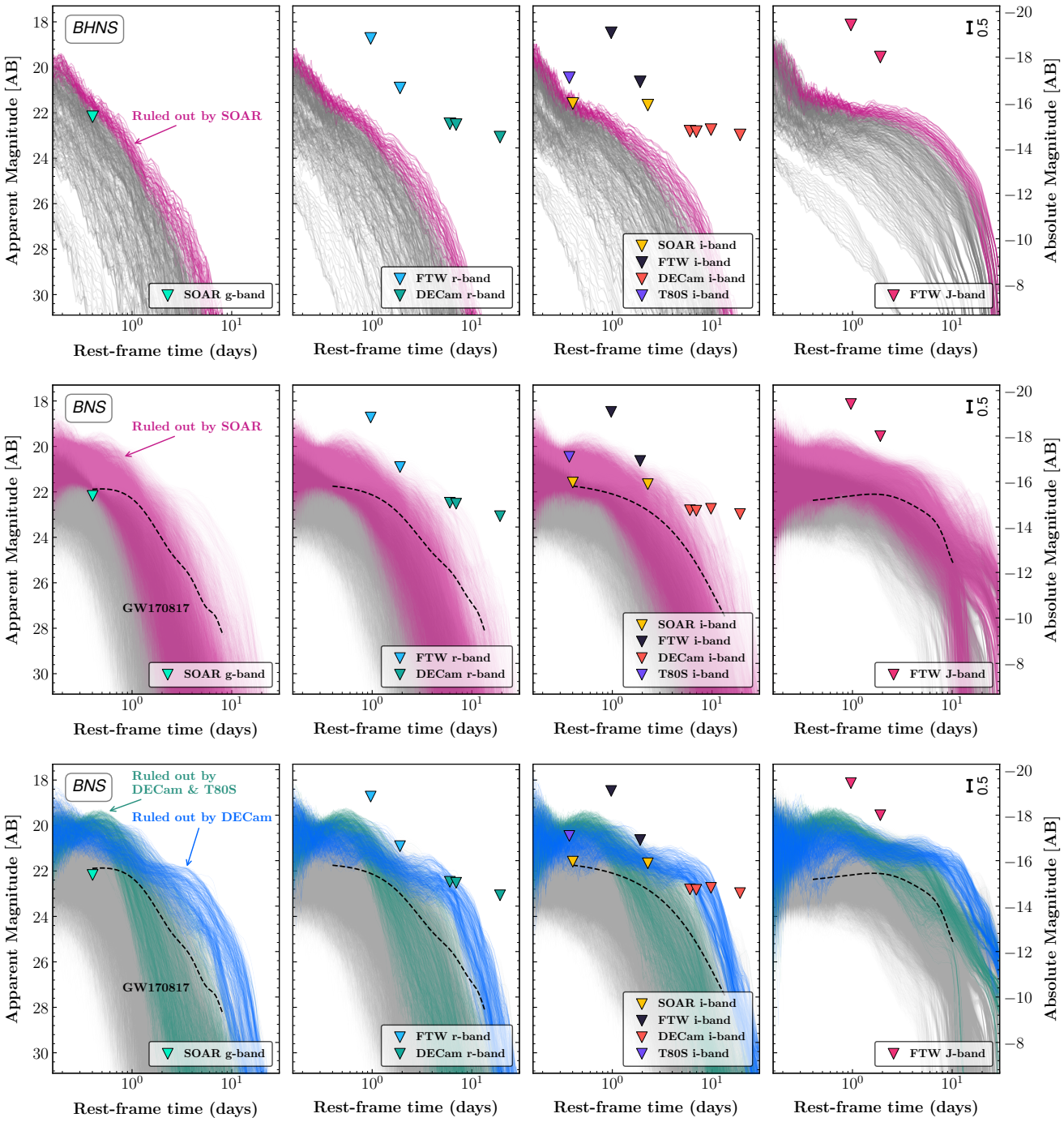

Figure 3. Kilonova light-curve simulations for BHNS (top row) and BNS (middle and bottom rows) at a distance of 323 Mpc. Each panel shows rest-frame synthetic light curves in a different photometric band, with observed upper limits overlaid as colored triangles. The full ensemble of model predictions is shown in gray. Magenta-highlighted curves indicate models ruled out by SOAR/Goodman galaxy-targeted observations, while blue-highlighted curves mark models disfavored by DECam observations. Green-highlighted curves correspond to the models additionally ruled out jointly by the addition of T80S observations to the DECam ones. For reference, the light curves of AT 2017gfo (scaled to a distance of 323 Mpc) are shown as dashed black lines. The multiband photometry data of AT 2017gfo are taken from V. A. Villar et al. (2017), and a simple Gaussian process fit is applied to produce smoothed curves for display purposes. We note that uncertainties in the distance translate into vertical shifts in the apparent magnitudes of the model light curves. To illustrate this, we include a 0.5 mag reference scale in the corner of the last panel of each row, representing to first order the apparent magnitude shift corresponding to a 1σ uncertainty in distance.

4.3.1. Constraints for BHNS Scenarios

In the top row of Figure 3, we show the BHNS kilonova models in *griJ* bands. It is clear that the BHNS models can only be constrained by the SOAR *g*-band observations, and marginally by the SOAR *i* band. Overall, 15% of the models are disfavored by the SOAR data. Had the DECam observations been possible at the same time as the SOAR ones instead of 6 days later, they would have ruled out 51% of BHNS models over a significantly larger high-probability area, showing the importance of early observations.

The top panel of Figure 4 shows the constraints from SOAR on the BHNS models. EOS numbers 1, 2, and 3 correspond to DD2 (M. Hempel & J. Schaffner-Bielich 2010), AP3 (A. Akmal et al. 1998), and SFHo+HDelta (A. Drago et al. 2014)

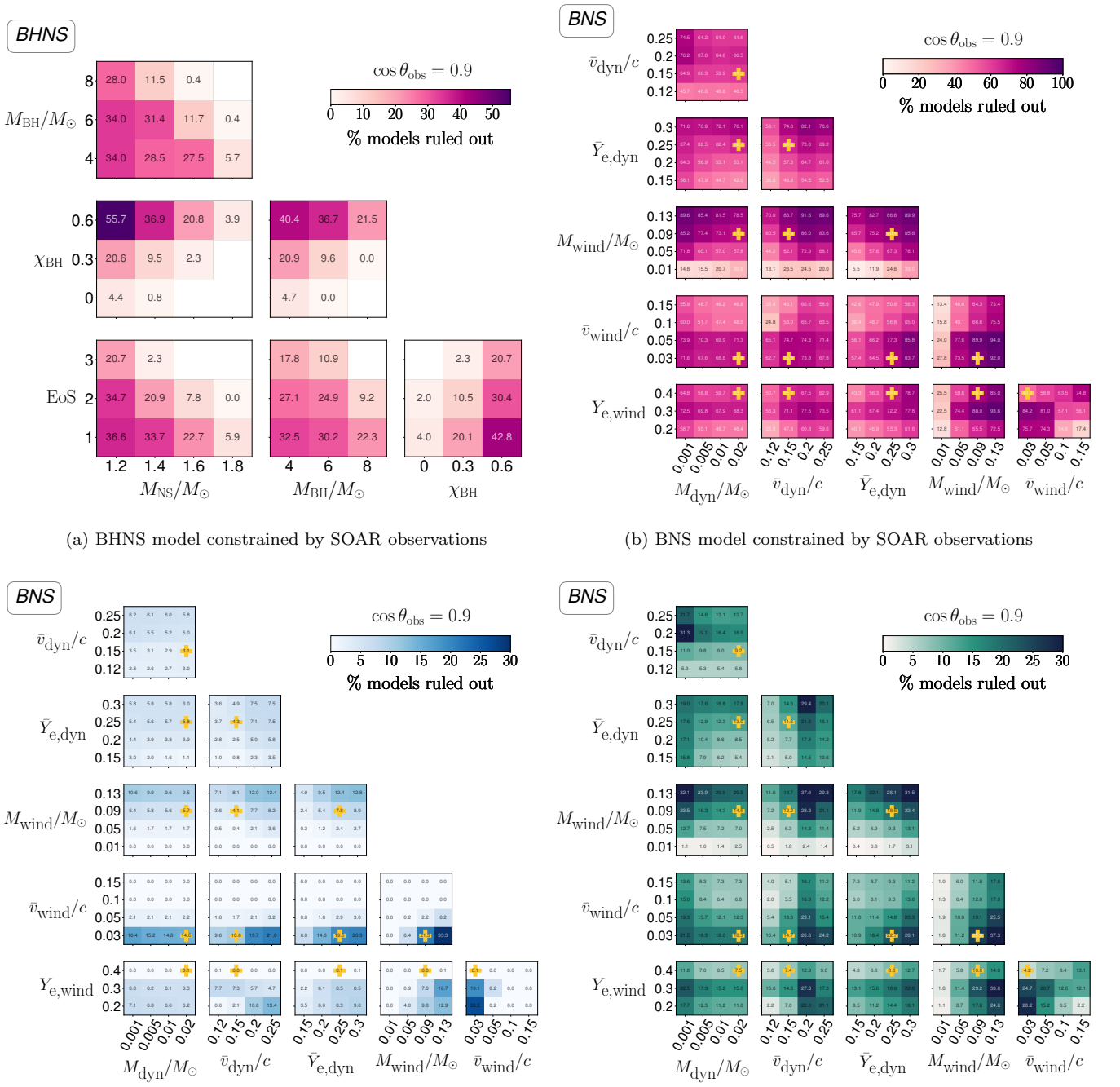

(a) BHNS model constrained by SOAR observations

(b) BNS model constrained by SOAR observations

(c) BNS model constrained by DECam observations

(d) BNS model constrained by DECam and T80S observations

Figure 4. Corner plot showing the fraction of BHNS and BNS models ruled out by our observations with a viewing angle θ with $\cos(\theta) = 0.9$, represented by a color bar. The number labeled on each cell represents the overall exclusion fraction (%), conditional on given model parameters, computed by averaging over sampled distances. For BNS models, the yellow plus sign indicates the best-fit parameters of AT 2017gfo from R. Farinelli et al. (2025).

respectively, going from stiffer to softer. As expected, the largest fraction of models ruled out lies in the lowest neutron star mass bin and stiffer EOS, since in this case the neutron star is expected to be more easily disrupted by the black hole, producing a brighter counterpart. With a DD2 EOS and a $\sim$1.2 $M_\odot$ neutron star, about 37% of our models are excluded. From 21% to 56% of our models are excluded for our highest spinning black holes, at a 0.6 dimensionless spin magnitude, and a 1.2–1.6 $M_\odot$ neutron star. This is due to the ISCO radius reduction for highly spinning black holes compared to the nonspinning case, leading to more favorable disruption of the neutron star around it. About 0%–39% (where the range is due to the EOS considered; if one accounts for all EOSs, then this number is 28%) of models with black holes in the mass gap are also excluded, which is a larger fraction than those at higher masses, as they will also have a larger ISCO.

4.3.2. Constraints for BNS Scenarios

In the middle and bottom rows of Figure 3 we show the BNS kilonova light curves along with those ruled out by SOAR and DECam observations, respectively. A larger fraction of models can be ruled out in this case by both

follow-up campaigns. Again, the early SOAR g-band observations exclude the largest fraction of kilonova models (55%), though over a much smaller area than the DECam observations, which in this case constrain 1.4% of the kilonova models thanks to the deep i-band pointings. The models excluded by the DECam follow-up compose 43% of all the kilonova models at least as bright as AT 2017gfo, the kilonova associated with GW170817, within the first week after merger,[30] whereas SOAR observations rule out the full set of such kilonova models. At 6 days post-merger, the kilonova is expected to be redder than earlier epochs, e.g., AT 2017gfo had an $r-i$ color of $\sim$0.10 mag at 0.5 days and $\sim$0.76 mag at 6 days (V. A. Villar et al. 2017), which, coupled to our deeper limits in i compared to r, rendered our i band depths more constraining. DECam + T80S jointly rule out 4% of the kilonova models, which compose 48% of all the kilonova models at least as bright as AT 2017gfo.

The FTW observations, which were galaxy targeted over the northern high-probability region of the sky map, correspond to a luminosity distance of 383 $\pm$ 96 Mpc. Assuming that the event occurred at the optimistic closest 1σ end of the distance distribution, i.e., 287 Mpc, the FTW data would marginally constrain kilonova models—ruling out the brightest $\sim$0.1% models at $\sim$1 day post-merger.

In the bottom panels of Figure 4, the SOAR observations rule out a large fraction of BNS kilonova models, about 90% of massive ($M_{\rm wind} \gtrsim 0.09\,M_\odot$) slow winds ($\bar{v}_{\rm wind} < 0.1c$). This is because, as expected, the larger wind ejecta mass gives rise to the brighter kilonovae that we can exclude, while the slower wind ejecta give rise to the longer-lasting emission. Large electron fractions are also significantly excluded by our observations (70% of models with $\bar{Y}_{e,\rm dyn} \gtrsim 0.2$ and $Y_{e,\rm wind} \gtrsim 0.3$). These models are in fact expected to give rise to blue, short-lived kilonovae that are well constrained by the early deep SOAR g-band limits.

The DECam observations also rule out a significant fraction of massive ($M_{\rm wind} \gtrsim 0.09\ M_\odot$), slow ($\bar{v}_{\rm wind} \sim 0.03c$) wind ejecta, albeit for a smaller number of models ($\sim$30% for DECam and DECam+T80S). We also find a slight trend where a larger fraction of models are ruled out at lower dynamical ejecta masses ($M_{\rm dyn} \lesssim 0.001\,M_\odot$) compared to higher masses, as smaller dynamical ejecta lead to a reduced "shielding" effect on the inner wind ejecta, resulting in a brighter kilonova (K. Kawaguchi et al. 2020). This is also observed at the larger viewing angles explored in this work. As opposed to the SOAR case, the DECam limits do not have significant constraining power on the highest wind electron fraction $Y_{e,\rm wind} \sim 0.4$ (ruling out less than 1% of models since they lack the early blue observations), but they are relatively more constraining at $Y_{e,\rm wind} \lesssim 0.3$ (rejecting $\sim$7%) thanks to the late i-band observations. Combining DECam and T80S increases the exclusion fractions to 8% and 15% for $Y_{e,\rm wind} \sim 0.4$ and $Y_{e,\rm wind} \lesssim 0.3$, respectively. We do not show kilonova constraints for the FTW observations, as they can only constrain a few models at the low-end tail of the luminosity distance posterior owing to the shallow depths reached in poor observing conditions.

[30] The time window (within one week post-merger) was chosen to encompass the SOAR observing period and the first (most constraining) DECam epoch. Beyond this period, an AT 2017gfo−like kilonova at 323 Mpc typically fades too much in optical bands to be detectable by ground-based telescopes.

5. Discussion

Overall, we find that our constraints show a smaller exclusion fraction for BHNS than for BNS models. This finding is not surprising, as the BHNS scenarios we consider are typically fainter than BNSs. The BHNS kilonovae used in our work go down to ejecta masses of $10^{-4}\,M_\odot$ (L. W. P. Mathias et al. 2024), which is about an order of magnitude below the lowest value we assume for BNSs. Moreover, the BHNS kilonova is expected to lack a polar dynamical ejecta component, as reflected by our models, so an on-axis observer is more likely to be able to observe a brighter BNS than BHNS kilonova, all kilonova parameters but the squeezed polar component being equal.

The angular dependence of the models we use is such that the most stringent constraints are obtained for on-axis systems. Since the lanthanide-rich ejecta are launched around the plane of the binary within some angle, emission from kilonovae observed edge-on will face a larger optical depth than those observed on-axis and will therefore appear significantly fainter (e.g., M. Bulla 2019; S. Darbha & D. Kasen 2020; O. Korobkin et al. 2021; L. W. P. Mathias et al. 2024). We show kilonova constraints at different viewing angles in Appendix C. We note that results in the $\cos(\theta_{\rm obs}) = 0.9$ scenario are qualitatively similar to but less stringent (in terms of model constraints) than the on-axis case.

6. Conclusions

We have presented our observational campaign aimed at identifying a kilonova associated with the high-significance GW event candidate S250206dm, which is a probable BHNS or BNS merger. In the BHNS case, this event is interesting in light of the possibility that the black hole had a low mass, 3–5 $M_\odot$, which would place it within the mass gap, as well as increasing the likelihood of an EM counterpart as compared to other BHNS systems. This event likely represents the most exciting event of LIGO/Virgo/KAGRA O4 so far for multimessenger searches, given its low false-alarm rate and significant probability of having ejected matter outside of the remnant ISCO.

Our follow-up campaign for S250206dm combined coordinated observational efforts from optical to near-infrared, using facilities in both hemispheres, including DECam, T80-South, SOAR, and FTW. Prompt galaxy-targeted observations were carried out with SOAR and FTW within hours of the GW trigger. We also performed wide-field imaging follow-up with DECam and T80S, reaching depth down to $r/i \sim 23$ mag from hours to weeks post-merger, covering a substantial fraction of the southern sky localization region of S250206dm.

Although no convincing kilonova candidates were identified in our follow-up observations, we place competitive constraints on kilonova models associated with S250206dm given our competitive depths. Under the assumption of an off-axis viewing angle with $\cos(\theta) = 0.9$, assuming that this event is a mass-gap BHNS, we rule out up to $\sim$40% of simulated models conditional on the neutron star mass and EOS around the top 33 host galaxies in the southern lobe of this event's localization. Assuming BNS kilonovae described by M. Bulla (2023) instead, we are able to rule out about 90% of models for galaxies with massive ($\gtrsim$0.09 $M_\odot$) and slow ($\bar{v}_{\rm wind} < 0.1c$) wind ejecta. 74% of models with wind ejecta mass $\gtrsim$0.05 $M_\odot$ are also excluded.

Our DECam (DECam + T80S) constraints, on the other hand, cover ∼9.3% (4.5%) of the sky probability and constrain ∼43% (48%) of BNS models brighter or similar to the GW170817 kilonova. Combined with ZTF limits, kilonova models brighter than −15 mag that rise (with evolution rate $\alpha < 0$ mag day^{-1}), as well as those brighter than −16.5 mag slowly fading ($\alpha > 0.3$ mag day^{-1}), can be ruled out over the majority (77%) of the sky probability of this event, as detailed in T. Ahumada et al. (2025a). Placing these competitive constraints on kilonova emission is extremely important to inform the future strategies of GW follow-up, as well as to understand the kilonova luminosity function (M. M. Kasliwal et al. 2020).

Compared to previous multimessenger campaigns for neutron star mergers, such as the work of S. Anand et al. (2021), which derived kilonova constraints for BHNS mergers in O3, our results deliver more stringent model constraints in general. For example, their limits only ruled out some massive ejecta ($>0.05\,M_{\odot}$) models at the lower end of the luminosity distance estimate for S200115j, while S200105ae (later deemed a subthreshold event) follow-up did not allow for any constraint of kilonova models. Thanks to early and deep DECam observations, tighter constraints were possible on GW190814 (I. Andreoni et al. 2020; R. Morgan et al. 2020; S. Anand et al. 2021); however, GW190814 is likely a binary black hole merger and thus may not have produced a kilonova (R. Abbott et al. 2020; I. Tews et al. 2021).

In the case of S250206dm, if DECam observations had been allowed on the day of trigger and a similar depth was reached, 51% of our BHNS and 82% of our BNS models would have been constrained. This work shows the potential for detection of kilonovae associated with both BNS and BHNS mergers at distances >300 Mpc, provided that deep and prompt observations can be carried out. Given the typical BNS/NSBH multimessenger event distances expected for the next LIGO/Virgo/KAGRA observing run (O5, anticipated to start in 2028), reaching out to ∼1 Gpc (R. Kaur et al. 2024; K. Kunumkai et al. 2024b), this finding shows the promise of DECam follow-up observations in finding the next GW EM counterpart in the coming years.

Acknowledgments

L.H., T.C., and A.P. acknowledge that this material is based on work supported by NSF grant No. 2308193. B.O. gratefully acknowledges support from the McWilliams Postdoctoral Fellowship at Carnegie Mellon University. M.B. acknowledges the Department of Physics and Earth Science of the University of Ferrara for the financial support through the FIRD 2024 grant. I.A. acknowledges support from the National Science Foundation Award AST 2505775 and NASA grant 24-ADAP24-0159. This work was supported by the Deutsche Forschungsgemeinschaft (DFG, German Research Foundation) under Germany's Excellence Strategy—EXC-2094—390783311. M.W.C. acknowledges support from the National Science Foundation with grant Nos. PHY-2117997, PHY-2308862, and PHY-2409481.

This work used resources on the Vera Cluster at the Pittsburgh Supercomputing Center (PSC). We thank the PSC staff for help with setting up our software on the Vera Cluster.

This project used data obtained with the Dark Energy Camera (DECam), which was constructed by the Dark Energy Survey (DES) collaboration. Funding for the DES Projects has been provided by the US Department of Energy, the US National Science Foundation, the Ministry of Science and Education of Spain, the Science and Technology Facilities Council of the United Kingdom, the Higher Education Funding Council for England, the National Center for Supercomputing Applications at the University of Illinois at Urbana-Champaign, the Kavli Institute for Cosmological Physics at the University of Chicago, the Center for Cosmology and Astro-Particle Physics at The Ohio State University, the Mitchell Institute for Fundamental Physics and Astronomy at Texas A&M University, Financiadora de Estudos e Projetos, Fundação Carlos Chagas Filho de Amparo à Pesquisa do Estado do Rio de Janeiro, Conselho Nacional de Desenvolvimento Científico e Tecnológico and the Ministério da Ciência, Tecnologia e Inovação, the Deutsche Forschungsgemeinschaft, and the Collaborating Institutions in the Dark Energy Survey.

The Collaborating Institutions are Argonne National Laboratory, the University of California at Santa Cruz, the University of Cambridge, Centro de Investigaciones Enèrgeticas, Medioambientales y Tecnològicas-Madrid, the University of Chicago, University College London, the DES-Brazil Consortium, the University of Edinburgh, the Eidgenössische Technische Hochschule (ETH) Zürich, Fermi National Accelerator Laboratory, the University of Illinois at Urbana-Champaign, the Institut de Ciéncies de l'Espai (IEEC/CSIC), the Institut de Física d'Altes Energies, Lawrence Berkeley National Laboratory, the Ludwig-Maximilians Universität München and the associated Excellence Cluster Universe, the University of Michigan, NSF's NOIRLab, the University of Nottingham, The Ohio State University, the OzDES Membership Consortium, the University of Pennsylvania, the University of Portsmouth, SLAC National Accelerator Laboratory, Stanford University, the University of Sussex, and Texas A&M University.

Based on observations at Cerro Tololo Inter-American Observatory, NSF's NOIRLab (NOIRLab Prop. ID 2023B-851374; PI. Andreoni & Palmese), which is managed by the Association of Universities for Research in Astronomy (AURA) under a cooperative agreement with the National Science Foundation. We thank Kathy Vivas, Alfredo Zenteno, and CTIO staff for their support with DECam observations. Some of the observations reported in this paper were obtained with the Southern African Large Telescope (SALT).

This research has made use of the NASA/IPAC Extragalactic Database (NED), which is funded by the National Aeronautics and Space Administration and operated by the California Institute of Technology.

Facilities: Blanco, SOAR, WO:2m, SALT.

Software: Astropy (Astropy Collaboration et al. 2013, 2018, 2022), SciPy (P. Virtanen et al. 2020), Numpy (C. R. Harris et al. 2020), MatPlotLib (J. D. Hunter 2007), CuPy (R. Okuta et al. 2017), Scikit-image (S. Van der Walt et al. 2014), SourceExtractor (E. Bertin & S. Arnouts 1996), SWarp (E. Bertin 2010), SFFT (L. Hu et al. 2021), dustmap (G. M. Green 2018), ligo.skymap (L. P. Singer et al. 2016a, 2016b), healpy (A. Zonca et al. 2019), TreasureMap (S. D. Wyatt et al. 2020).

Appendix A
Candidates from DECam Search

Our pipeline executed an automated filtering process on transient candidates with at least one alert. (i) Not stellar: We excluded stellar objects by cross-matching with the Gaia DR3

Table 1
Candidate Filtering Results for DECam Search

Vetting Filter	Number Passed	Fraction Passed
Regular pipeline cuts		
Alert produced on difference image	608,054	1.00
Not stellar in Gaia/DELVE	77,094	0.115
Not MPC object	77,094	0.115
Real/bogus score $\geqslant$0.7	40,645	0.061
Event-based cuts		
Discovered in the first night	16,750	0.025
Multiple detections	3589	0.005
Visual inspection	37	6.1×10^{-5}
Fast decline in the light curve	2	3.0×10^{-6}
No previous history	1	1.5×10^{-6}
Red color in the light curve	**0**	0

Note. The quantities listed in the table represent the number of objects that passed each step in the filtering process. Due to limited coverage of the observed sky fields, the MPC database was insufficient for removing moving objects in this case.

and DELVE catalogs, removing sources flagged as stars based on proper motion in Gaia and morphological classification in DELVE. (ii) Not MPC: The pipeline accessed the Minor Planet Center (MPC) database to eliminate known moving objects. (iii) Not artifact: We then required that each transient candidate include at least one high-confidence detection with a real/bogus score $\geqslant$0.7. The results of the automated filtering process are outlined in Table 1. We note that the automated vetting process eliminated over 90% of the initial transient candidates.

We then applied a series of event-based vetting criteria to the remaining candidates to identify potential counterparts of S250206dm. These criteria included the following: (i) Early detection: the candidate must have been discovered during the first night of observations.[31] (ii) Multiple detections: candidates with only one detection in the difference image were excluded, as such detections are likely spurious or caused by moving objects. (iii) Visual inspection: we visually inspected the subtractions and light curves to further exclude artifacts and probable variable stars. (iv) Fading behavior: we computed the steepest decline rate in the candidate's light curve across the four DECam epochs and retained only those with a decline rate >0.3 mag/day. (v) No prior variability: we checked the DECam archive, ATLAS forced photometry, and the Transient Name Server (TNS) to ensure that there was no previous variability for the candidate. (vi) Red color: we required a red color, $r - i > 0$, in the light curve after correcting for Milky Way extinction, as expected for a plausible kilonova at 6 days post-merger. The results of the event-based filtering are summarized in Table 1.

Table 2 lists the candidates that passed visual inspection from the DECam search. Most of the candidates were excluded because of their slow photometric evolution during our observations (i.e., <0.3 mag day^{-1}). Of the two remaining sources, AT 2025me had previous variability, which was reported prior to the event S250206dm; AT 2025bno is a hostless transient rejected by its blue color.

Table 2
Candidates from DECam Search

Candidate	Coordinates (R.A., Decl.)	Discov. Mag.	Discov. Color Mag.	Phot. Evol.	Redshift	Comment
		Fast Decline				
AT 2025bno	16:10:47.65 −68:28:13.6	$i = 21.10$	$r - i = -0.18$ (−0.23)	$\geqslant 0.52$ (i)	...	Hostless
AT 2025me	16:49:43.68 −70:23:34.2	$r = 18.90$	$r - i = -0.11$ (−0.16)	0.94 (r)	...	Pre-event detection
		Flat or Slowly Decline				
AT 2025bmy	15:42:37.02 −69:36:49.6	$i = 21.28$	$r - i = 0.97$ (0.92)	0.07 (i)	...	...
AT 2025bnh	16:32:38.20 −68:31:02.9	$r = 22.54$	$r - i = 0.96$ (0.90)	0.11 (r)	0.140 $_{\rm SALT}$	Nuclear
AT 2025bmw	16:18:12.69 −71:56:17.4	$r = 21.24$	$r - i = 0.88$ (0.83)	0.09 (r)	...	Nuclear
AT 2025bnb	15:50:13.08 −70:19:04.8	$i = 20.87$	$r - i = 0.80$ (0.72)	0.04 (i)	0.117 $_{\rm NED}$	...
AT 2025bnt	16:33:49.52 −70:02:56.8	$i = 21.36$	$r - i = 0.78$ (0.73)	0.10 (r)	...	...
AT 2025bmx	15:57:20.48 −68:40:02.4	$i = 21.40$	$r - i = 0.72$ (0.66)	0.07 (i)	...	Nuclear
AT 2025btj	16:06:31.80 −66:57:35.3	$i = 22.06$	$r - i = 0.65$ (0.59)	0.02 (i)	...	Hostless
AT 2025bts	16:45:09.06 −71:31:23.2	$i = 22.61$	$r - i = 0.64$ (0.59)	0.04 (i)	...	...
AT 2025bnu	16:51:27.56 −69:06:28.5	$r = 22.04$	$r - i = 0.59$ (0.54)	0.21 (r)	...	Nuclear
AT 2025bnp	15:52:22.31 −70:04:42.6	$i = 21.68$	$r - i = 0.53$ (0.46)	−0.02 (i)	0.100 $_{\rm SALT}$	...
AT 2025fso	15:30:50.47 −70:27:21.7	$i = 21.99$	$r - i = 0.51$ (0.44)	0.24 (r)	...	...
AT 2025bnc	17:05:02.58 −69:52:26.0	$r = 22.62$	$r - i = 0.49$ (0.43)	0.06 (i)	...	Hostless
AT 2025fsy	16:26:53.13 −70:00:47.0	$i = 21.89$	$r - i = 0.47$ (0.41)	0.05 (r)	...	Nuclear
AT 2025bms	16:28:24.40 −70:48:57.9	$r = 22.13$	$r - i = 0.42$ (0.37)	0.23 (r)	...	Nuclear
AT 2025fsq	15:57:15.75 −67:45:22.5	$i = 22.48$	$r - i = 0.41$ (0.35)	0.09 (i)	...	Nuclear
AT 2025bns	16:52:25.99 −69:04:18.6	$r = 22.84$	$r - i = 0.39$ (0.34)	0.09 (r)	...	...
AT 2025bni	16:33:59.30 −69:18:09.3	$r = 22.58$	$r - i = 0.34$ (0.27)	0.08 (r)	...	Nuclear
AT 2025fsx	15:43:23.69 −68:44:52.3	$i = 22.48$	$r - i = 0.30$ (0.24)	−0.03 (i)	...	...
AT 2025bth	16:52:03.71 −68:14:22.3	$r = 20.40$	$r - i = 0.14$ (0.10)	0.10 (i)	0.102 $_{\rm NED}$	...
AT 2025bnj	15:59:51.07 −66:55:46.9	$i = 21.68$	$r - i = 0.06$ (0.01)	0.01 (i)	0.140 $_{\rm SALT}$	...

[31] Our DECam observations reached similar depths across the first three epochs; thus, requiring detection on the first night is a reasonable criterion for identifying a fading counterpart.

Table 2
(Continued)

Candidate	Coordinates (R.A., Decl.)	Discov. Mag.	Discov. Color Mag.	Phot. Evol.	Redshift	Comment
AT 2025fsz	16:32:30.65 −68:42:58.8	$r = 23.23$	$r - i = 0.00$ (−0.05)	0.04 (i)	...	Nuclear
AT 2025fsw	15:47:15.50 −67:28:05.4	$i = 22.39$	$r - i = -0.05$ (−0.11)	0.29 (r)	...	Hostless
AT 2025fst	16:32:39.71 −69:37:24.2	$i = 23.09$	$r - i = -0.06$ (−0.13)	0.07 (i)	...	Hostless
AT 2025fsu	16:28:42.95 −71:20:20.6	$r = 22.85$	$r - i = -0.12$ (−0.17)	0.01 (r)	...	...
AT 2025fta	16:11:52.15 −70:52:38.4	$i = 22.82$	$r - i = -0.13$ (−0.19)	0.05 (i)	...	Hostless
AT 2025fsr	15:44:27.41 −68:10:13.6	$i = 22.89$	$r - i = -0.13$ (−0.19)	0.01 (r)	...	...
AT 2025bnv	15:43:42.28 −67:40:57.0	$i = 21.11$	$r - i = -0.15$ (−0.22)	0.08 (i)	...	...
AT 2025btc	16:06:40.98 −70:59:27.9	$i = 22.14$	$r - i = -0.18$ (−0.24)	0.06 (r)	...	...
AT 2025fss	16:01:18.31 −70:59:41.1	$i = 21.60$	$r - i = -0.21$ (−0.27)	0.01 (i)	...	...
AT 2025fsp	15:50:54.92 −70:26:25.3	$i = 23.26$	$r - i = -0.26$ (C0.34)	0.28 (r)	...	...
AT 2024aexy	16:07:47.10 −67:06:08.4	$i = 21.23$	$r - i = -0.29$ (−0.34)	0.09 (r)	...	Pre-event detection
AT 2025bnm	16:22:52.18 −69:01:23.7	$i = 22.04$	$r - i = -0.38$ (−0.44)	0.04 (i)	...	...
AT 2025bmz	16:40:26.39 −66:46:25.6	$r = 19.83$	...	0.08 (r)	0.053 $_{\rm NED}$	Nuclear
AT 2025btr	16:58:02.83 −68:26:49.5	$i = 22.29$	...	0.07 (i)	...	...
AT 2025fsv	16:48:20.86 −67:14:02.0	$i = 22.60$	...	0.06 (i)	...	Hostless

Appendix B
Spectroscopic Follow-up with SALT

We obtained long-slit optical spectroscopic observations of optical transients (and their host galaxies) potentially associated with S250206dm with the 10 m class SALT (D. A. H. Buckley et al. 2006) at Sutherland Observatory in Sutherland, South Africa. Observations were obtained through a SALT Gravitational Wave Director's Discretionary Time proposal (ID: 2024-2-GWE-001; PI: T. Cabrera). Long-slit spectroscopy of four candidates, AT 20205bnt (2025 February 17), AT 2025bnj (2025 February 15 and 16), AT 2025bnp (2025 February 14), and AT 2025bnh (2025 February 22), was acquired with the Robert Stobie Spectrograph (RSS; E. B. Burgh et al. 2003). Due to the poor visibility of these fields to SALT at the time of the observations, only a single target was able to be observed per night. Data were obtained between 2025 February 14 and 22. The observation of AT 2025bnj was repeated, as the initial data did not satisfy our observing condition requirements.

Each spectrum was obtained using the PG0700 grating at a grating angle of $4\overset{\circ}{.}6$ (corresponding to a camera angle of $22\overset{\circ}{.}75$) with the PC03400 blocking filter using a slit width of $1\overset{''}{.}5$. The spectra covered the observer-frame wavelength range 3592−7479 Å with resolution $R = 735$ at the central wavelength of 5580 Å. We used an exposure time of 1×900 s per target.

The data were reduced using the RSS long-slit spectra processing and extraction app `rsslsspectra` (User Guide: https://astronomers.salt.ac.za/wp-content/uploads/sites/71/2024/09/rsslsspectra.pdf). We extracted traces associated with the host galaxy of these transients. We searched by eye for narrow emission features in the spectra for all targets, finding at least two regions associated with Hα, Hβ, O[II], or O[III] lines in each of the spectra of AT 2025bnj, AT 2025bnp, and AT 2025bnh, estimating best-fit redshifts of 0.140 ± 0.001, 0.100 ± 0.01, and 0.140 ± 0.001, respectively. There were no discernible features in the spectrum for AT 20205bnt, and so we were unable to measure a redshift for this target. The results of SALT follow-up spectroscopy are summarized in Table 3.

Table 3
SALT Spectroscopy for S250206dm

TNS ID	SALT Obs. Date	Identified Lines	Redshift	Notes
AT 2025bnp	2025-02-14	Hα, Hβ, O[III]	0.1 ± 0.01	Low SNR, increased uncertainty in line identification
AT 2025bnj	2025-02-15	Hβ, O[II], O[III]	0.14 ± 0.001	Observing conditions unfavorable
AT 2025bnj	2025-02-16	Hβ, O[II], O[III]	0.14 ± 0.001	Repeat observation
AT 2025bnt	2025-02-17	⋯	⋯	No lines identified
AT 2025bnh	2025-02-22	Hβ, O[II], O[III]	0.14 ± 0.001	⋯

Note. See the text for details on the instrumental configuration, which was identical for all spectra.

Appendix C
Kilonova Constraints with a Different Viewing Angle

In Figure 4 we show the kilonova model constraints for a fiducial viewing angle of 25°. In Figure 5, we show the same results but now considering a range of viewing angles between 0° and 45°. Viewing angles of 45°–90° are roughly similar, as they are dominated by faint emission from the lanthanide-rich dynamical ejecta and are less sensitive to the wind ejecta, which for edge-on systems is therefore mostly screened. In fact, it is clear from Figure 5 how the constraints of the wind ejecta parameters are significantly sensitive to variations in viewing angle, while the dynamical ejecta parameters are less sensitive.

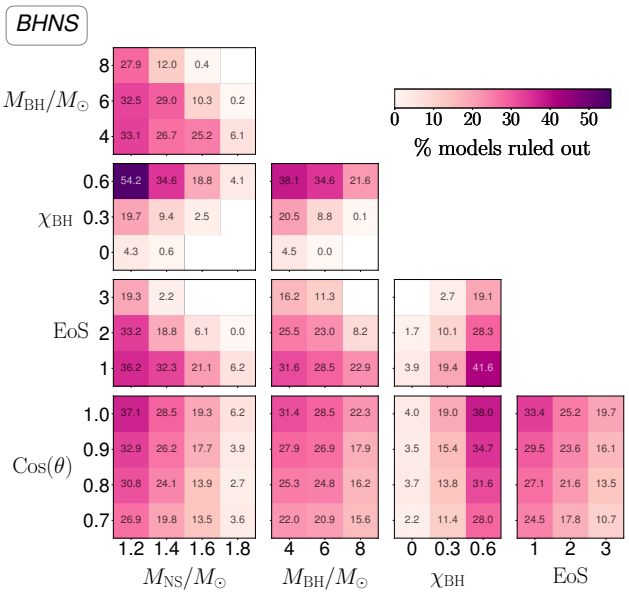

(a) BHNS model constrained by SOAR observations

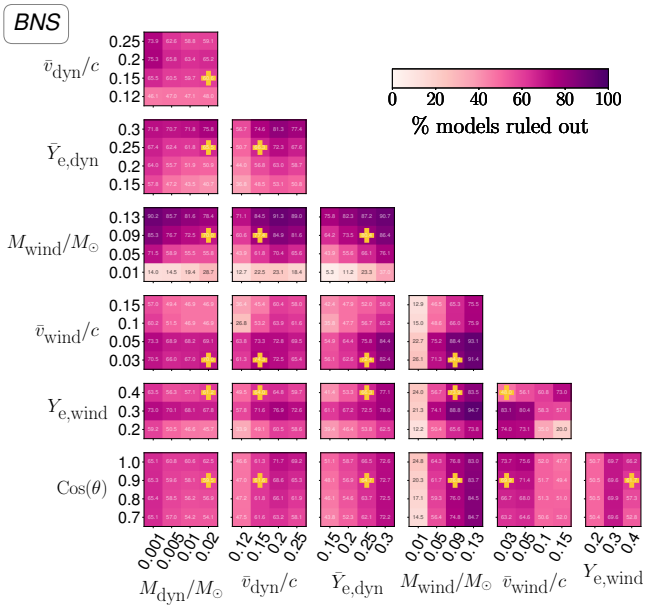

(b) BNS model constrained by SOAR observations

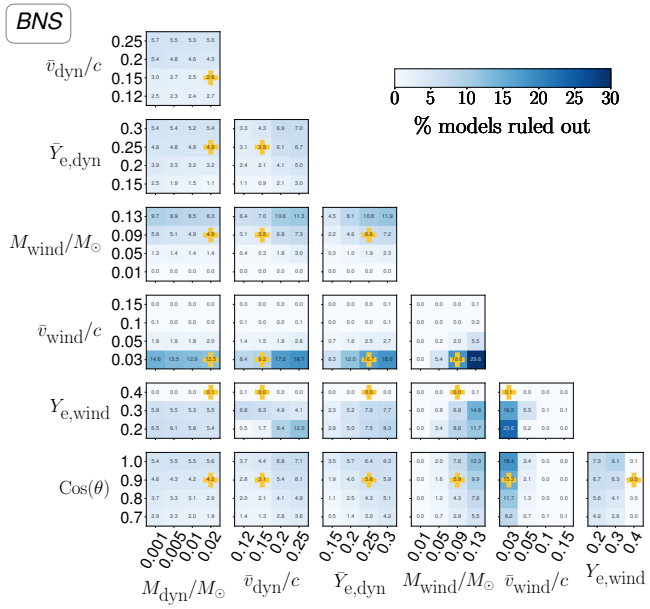

(c) BNS model constrained by DECam observations

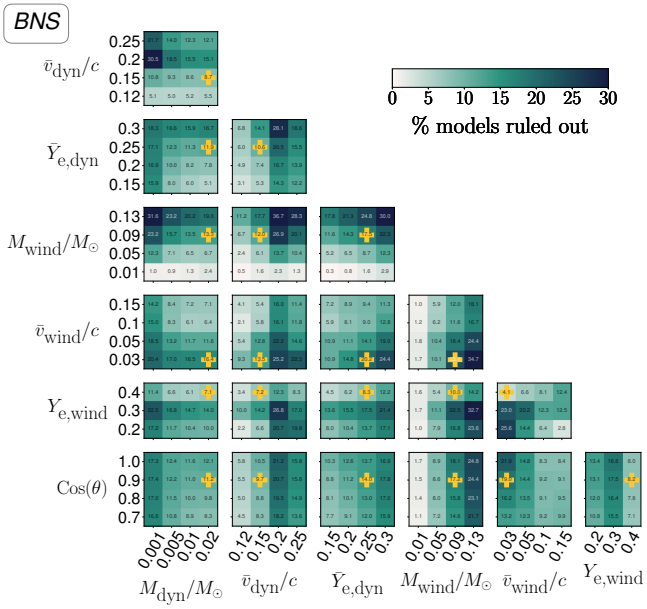

(d) BNS model constrained by DECam and T80S observations

Figure 5. Corner plots similar to those in Figure 4 showing the fraction of BHNS and BNS models ruled out by our observations, but here with a range of different viewing angles. For visualization purposes we only show models to viewing angles of 0°–45°, since from 45° and above the fractions stay roughly similar.

ORCID iDs

Lei Hu https://orcid.org/0000-0001-7201-1938
Tomás Cabrera https://orcid.org/0000-0002-1270-7666
Antonella Palmese https://orcid.org/0000-0002-6011-0530
James Freeburn https://orcid.org/0009-0006-7990-0547
Mattia Bulla https://orcid.org/0000-0002-8255-5127
Igor Andreoni https://orcid.org/0000-0002-8977-1498
Xander J. Hall https://orcid.org/0000-0002-9364-5419
Brendan O'Connor https://orcid.org/0000-0002-9700-0036
Ariel Amsellem https://orcid.org/0000-0003-3433-2698
Clécio R. Bom https://orcid.org/0000-0003-4383-2969
Malte Busmann https://orcid.org/0009-0001-0574-2332
Jennifer Fabà https://orcid.org/0009-0006-7670-9843
Julius Gassert https://orcid.org/0009-0008-2754-1946
Sena Kalabalik https://orcid.org/0009-0003-6582-8204
Keerthi Kunnumkai https://orcid.org/0009-0000-4830-1484
Daniel Gruen https://orcid.org/0000-0003-3270-7644
Luidhy Santana-Silva https://orcid.org/0000-0003-3402-6164
André Santos https://orcid.org/0000-0002-1420-3584
Tomás Ahumada https://orcid.org/0000-0002-2184-6430
Jonathan Carney https://orcid.org/0000-0001-8544-584X
Michael W. Coughlin https://orcid.org/0000-0002-8262-2924
Xingzhuo Chen https://orcid.org/0000-0003-3021-4897
K. E. Saavik Ford https://orcid.org/0000-0002-5956-851X
Daniel E. Holz https://orcid.org/0000-0002-0175-5064
Mansi M. Kasliwal https://orcid.org/0000-0002-5619-4938
Ignacio Magaña Hernandez https://orcid.org/0000-0003-2362-0459
Cassidy Mihalenko https://orcid.org/0009-0004-0322-6299
Rosalba Perna https://orcid.org/0000-0002-3635-5677
Arno Riffeser https://orcid.org/0000-0002-5466-3892
Julian Sommer https://orcid.org/0000-0002-1154-8317
Sarah Teague https://orcid.org/0009-0009-5634-4244
Pablo Vega https://orcid.org/0009-0008-0928-7884
Olga Volchansky https://orcid.org/0009-0008-1415-6678
Lifan Wang https://orcid.org/0000-0001-7092-9374
Yajie Zhang https://orcid.org/0000-0003-2976-8198

References

Abbott, B. P., Abbott, R., Abbott, T. D., et al. 2017, PhRvL, 119, 161101
Abbott, B. P., Abbott, R., Abbott, T. D., et al. 2020, ApJL, 892, L3
Abbott, R., Abbott, T. D., Abraham, S., et al. 2020, ApJL, 896, L44
Acernese, F., Agathos, M., Agatsuma, K., et al. 2014, CQGra, 32, 024001
Ahumada, T., Anand, S., Coughlin, M., et al. 2024, PASP, 136, 114201,
Ahumada, T., Anand, S., Bulla, M., et al. 2025a, arXiv:2507.00357
Ahumada, T., Karambelkar, V., Bellm, E., et al. 2025b, GCN, 39228, 1
Akmal, A., Pandharipande, V. R., & Ravenhall, D. G. 1998, PhRvC, 58, 1804
Anand, S., Coughlin, M. W., Kasliwal, M. M., et al. 2021, NatAs, 5, 46
Anand, S., Pang, P. T. H., Bulla, M., et al. 2023, arXiv:2307.11080
Andreoni, I., Goldstein, D. A., Kasliwal, M. M., et al. 2020, ApJ, 890, 131
Astropy Collaboration, Price-Whelan, A. M., Lim, P. L., et al. 2022, ApJ, 935, 167
Astropy Collaboration, Price-Whelan, A. M., Sipőcz, B. M., et al. 2018, AJ, 156, 123
Astropy Collaboration, Robitaille, T. P., Tollerud, E. J., et al. 2013, A&A, 558, A33
Becker, A., 2015 HOTPANTS: High Order Transform of PSF ANd Template Subtraction, Astrophysics Source Code Library, ascl:1504.004
Bertin, E. 2006, in ASP Conf. Ser. 351, Astronomical Data Analysis Software and Systems XV, ed. C. Gabriel et al. (San Francisco, CA: ASP), 112
Bertin, E., 2010 SWarp: Resampling and Co-adding FITS Images Together, Astrophysics Source Code Library, ascl:1010.068
Bertin, E., & Arnouts, S. 1996, A&AS, 117, 393
Bertin, E., Mellier, Y., Radovich, M., et al. 2002, in ASP Conf. Ser. 281, Astronomical Data Analysis Software and Systems XI, ed. D. A. Bohlender, D. Durand, & T. H. Handley (San Francisco, CA: ASP), 228
Buckley, D. A. H., Swart, G. P., & Meiring, J. G. 2006, Proc. SPIE, 6267, 62670Z
Bulla, M. 2019, MNRAS, 489, 5037
Bulla, M. 2023, MNRAS, 520, 2558
Burgh, E. B., Nordsieck, K. H., Kobulnicky, H. A., et al. 2003, Proc. SPIE, 4841, 1463
Busmann, M., Gruen, D., O'Connor, B., et al. 2025a, GCN, 39214, 1
Busmann, M., O'Connor, B., Sommer, J., et al. 2025b, arXiv:2503.14588
Cabrera, T., Hu, L., Hall, X., et al. 2025, GCN, 39318, 1
Cabrera, T., Palmese, A., Hu, L., et al. 2024, PhRvD, 110, 123029
Cardelli, J. A., Clayton, G. C., & Mathis, J. S. 1989, ApJ, 345, 245
Clemens, J. C., Crain, J. A., & Anderson, R. 2004, Proc. SPIE, 5492, 331
Cook, D. O., Ebert, R., Helou, G., et al. 2025a, GCN, 39185, 1
Cook, D. O., Ebert, R., Helou, G., et al. 2025b, GCN, 39235, 1
Cook, D. O., Mazzarella, J. M., Helou, G., et al. 2023, ApJS, 268, 14
Coughlin, M. W., Ahumada, T., Anand, S., et al. 2019, ApJL, 885, L19
Coulter, D. A. 2021, Teglon: A Pixel-level Gravitational Wave Search Optimization and Analysis Code v0.0.0, Zenodo, doi:10.5281/zenodo.5683508
Coulter, D. A., Kilpatrick, C. D., Andreoni, I., et al. 2025, GCN, 39303, 1
Dálya, G., Galgóczi, G., Dobos, L., et al. 2018, MNRAS, 479, 2374
Darbha, S., & Kasen, D. 2020, ApJ, 897, 150
Darc, P., Bom, C. R., Kilpatrick, C. D., et al. 2025, arXiv:2506.02224
Drago, A., Lavagno, A., Pagliara, G., & Pigato, D. 2014, PhRvC, 90, 065809
Farinelli, R., Cogato, F., Bulla, M., et al. 2025, JHEAp, submitted
Fernández, R., Foucart, F., Kasen, D., et al. 2017, CQGra, 34, 154001
Foucart, F. 2012, PhRvD, 86, 124007
Freeburn, J., Carney, J., Andreoni, I., & Cook, D. 2025a, GCN, 39196, 1
Freeburn, J., Teague, S., Carney, J., et al. 2025b, GCN, 39286, 1
Frostig, D., Karambelkar, V. R., Stein, R. D., et al. 2025, PASP, 137, 074203
Gössl, C. A., & Riffeser, A. 2002, A&A, 381, 1095
Green, G. M. 2018, JOSS, 3, 695
Harris, C. R., Millman, K. J., van der Walt, S. J., et al. 2020, Natur, 585, 357
Hempel, M., & Schaffner-Bielich, J. 2010, NuPhA, 837, 210
Hopp, U., Bender, R., Grupp, F., et al. 2014, Proc. SPIE, 9145, 91452D
Hu, L., Wang, L., & Chen, X. 2021, sfft v1.0.3, Zenodo, doi:10.5281/zenodo.5521634
Hu, L., Wang, L., Chen, X., & Yang, J. 2022, ApJ, 936, 157
Hunter, J. D. 2007, CSE, 9, 90
Kasen, D., Fernández, R., & Metzger, B. D. 2015, MNRAS, 450, 1777
Kasliwal, M. M., Anand, S., Ahumada, T., et al. 2020, ApJ, 905, 145
Kaur, R., O'Connor, B., Palmese, A., & Kunnumkai, K. 2024, arXiv:2410.10579
Kawaguchi, K., Kyutoku, K., Shibata, M., & Tanaka, M. 2016, ApJ, 825, 52
Kawaguchi, K., Shibata, M., & Tanaka, M. 2020, ApJ, 889, 171
Korobkin, O., Wollaeger, R. T., Fryer, C. L., et al. 2021, ApJ, 910, 116
Kunnumkai, K., Palmese, A., Bulla, M., et al. 2024a, arXiv:2409.10651
Kunnumkai, K., Palmese, A., Farah, A. M., et al. 2024b, arXiv:2411.13673
Kyutoku, K., Ioka, K., & Shibata, M. 2013, PhRvD, 88, 041503
Lang-Bardl, F., Bender, R., Goessl, C., et al. 2016, Proc. SPIE, 9908, 990844
Lattimer, J. M., & Schramm, D. N. 1974, ApJL, 192, L145
Levan, A. J., van Hoof, A., Martin-Carrillo, A., et al. 2025, GCN, 39218, 1
LIGO Scientific Collaboration 2015, CQGra, 32, 074001
LIGO Scientific CollaborationVirgo Collaboration, GBM, F., et al. 2017, ApJL, 848, L12
The LIGO Scientific Collaborationthe Virgo Collaborationthe KAGRA Collaboration 2024, ApJL, 970, L34
LIGO Scientific CollaborationVIRGO CollaborationKagra Collaboration 2025a, GCN, 39175, 1
Ligo Scientific CollaborationVIRGO CollaborationKagra Collaboration 2025b, GCN, 39178, 1
Ligo Scientific CollaborationVIRGO CollaborationKagra Collaboration 2025c, GCN, 39184, 1
Ligo Scientific CollaborationVIRGO CollaborationKagra Collaboration 2025d, GCN, 39231, 1
Margutti, R., & Chornock, R. 2021, ARA&A, 59, 155
Mathias, L. W. P., Di Clemente, F., Bulla, M., & Alessandro, D. 2024, MNRAS, 527, 11053
Metzger, B. D. 2019, LRR, 23, 1
Mooley, K. P., Deller, A. T., Gottlieb, O., et al. 2018, Natur, 561, 355
Morgan, R., Soares-Santos, M., Annis, J., et al. 2020, ApJ, 901, 83
Mukherjee, O., Hamburg, R. & Fermi-GBM Team 2025, GCN, 39183, 1
Nakar, E. 2020, PhR, 886, 1

Okuta, R., Unno, Y., Nishino, D., Hido, S., & Loomis, C. 2017, in Proc. Workshop on Machine Learning Systems (LearningSys) in The Thirty-first Annual Conf. Neural Information Processing Systems (NIPS), ed. U. Von Luxburg et al. (Red Hood, NY: Curran Associates) http://learningsys.org/nips17/assets/papers/paper_16.pdf
Onken, C. A., Wolf, C., Bessell, M. S., et al. 2024, PASA, 41, e061
Palmese, A., Kaur, R., Hajela, A., et al. 2024, PhRvD, 109, 063508
Perego, A., Radice, D., & Bernuzzi, S. 2017, ApJL, 850, L37
Pillas, M., Antier, S., Ackley, K., et al. 2025, arXiv:2503.15422
Radice, D., Perego, A., Hotokezaka, K., et al. 2018, ApJ, 869, 130
Ronchini, S., Bala, S., Wood, J., et al. 2024, ApJL, 970, L20
Rosswog, S., & Korobkin, O. 2024, AnP, 536, 2200306
Santos, A., Kilpatrick, C. D., Bom, C. R., et al. 2024, MNRAS, 529, 59
Schutz, B. F. 2011, CQGra, 28, 125023
Setzer, C. N., Peiris, H. V., Korobkin, O., & Rosswog, S. 2023, MNRAS, 520, 2829
Singer, L. P., Chen, H.-Y., Holz, D. E., et al. 2016a, ApJL, 829, L15
Singer, L. P., Chen, H.-Y., Holz, D. E., et al. 2016b, ApJS, 226, 10
Tews, I., Pang, P. T. H., Dietrich, T., et al. 2021, ApJL, 908, L1
Van der Walt, S., Schönberger, J. L., Nunez-Iglesias, J., et al. 2014, PeerJ, 2, e453
Villar, V. A., Guillochon, J., Berger, E., et al. 2017, ApJL, 851, L21
Virtanen, P., Gommers, R., Oliphant, T. E., et al. 2020, NatMe, 17, 261
Wyatt, S. D., Tohuvavohu, A., Arcavi, I., et al. 2020, ApJ, 894, 127
Zonca, A., Singer, L. P., Lenz, D., et al. 2019, JOSS, 4, 1298